The Astrophysical Journal Letters, 995:L63 (11pp), 2025 December 20 https://doi.org/10.3847/2041-8213/ae226c

ALMA Reveals Diverse Dust-to-gas Mass Ratios and Quenching Modes in Old Quiescent Galaxies

G. Lorenzon[1], D. Donevski[1,2], A. W. S. Man[3], M. Romano[4,5], K. E. Whitaker[6], S. Belli[7], D. Liu[8], M. M. Lee[9], D. Narayanan[10,11], A. Long[12,13], I. Shivaei[14], A. Nanni[1,15], K. Lisiecki[1], P. Sawant[1], G. Rodighiero[16], I. Damjanov[17], Junais[18,19], R. Davé[20,21], C. Pappalardo[22], C. Lovell[23], and M. Hamed[14]
[1] National Center for Nuclear Research, Pasteura 7, 02-093 Warsaw, Poland; giuliano.lorenzon@ncbj.gov.pl
[2] SISSA, Via Bonomea 265, 34136 Trieste, Italy
[3] Department of Physics & Astronomy, University of British Columbia, 6224 Agricultural Road, Vancouver, BC V6T 1Z1, Canada
[4] Max-Planck-Institut für Radioastronomie, Auf dem Hügel 69, 53121, Bonn, Germany
[5] INAF, OAPD, Vicolo dell'Osservatorio, 5, 35122 Padova, Italy
[6] Department of Astronomy, University of Massachusetts, Amherst, MA 01003, USA
[7] Dipartimento di Fisica e Astronomia, Università di Bologna, Bologna, Italy
[8] Purple Mountain Observatory, Nanjing, People's Republic of China
[9] DTU-Space, Technical University of Denmark, Elektrovej 327, DK-2800 Kgs. Lyngby, Denmark
[10] Department of Astronomy, University of Florida, 211 Bryant Space Sciences Center, Gainesville, FL, USA
[11] Cosmic Dawn Center (DAWN), Copenhagen, Denmark
[12] Department of Astronomy, University of Washington, Seattle, WA 98195-1700, USA
[13] Department of Astronomy, The University of Texas at Austin, 2515 Speedway Boulevard Stop C1400, Austin, TX 78712, USA
[14] Centro de Astrobiología (CAB), CSIC-INTA, Carretera de Ajalvir km 4, Torrejón de Ardoz 28850, Madrid, Spain
[15] INAF - Osservatorio Astronomico d'Abruzzo, Via Maggini SNC, 64100, Teramo, Italy
[16] Dipartimento di Fisica e Astronomia, Università di Padova, Vicolo dell'Osservatorio, 3, I-35122 Padova, Italy
[17] Department of Astronomy and Physics, Saint Mary's University, 923 Robie Street, Halifax, NS, B3H 3C3, Canada
[18] Instituto de Astrofísica de Canarias, Vía Láctea S/N, E-38205 La Laguna, Spain
[19] Departamento de Astrofísica, Universidad de La Laguna, E-38206 La Laguna, Spain
[20] Institute for Astronomy, Royal Observatory, University of Edinburgh, Edinburgh EH9 3HJ, UK
[21] Department of Physics & Astronomy, University of the Western Cape, Robert Sobukwe Road, Bellville, 7535, South Africa
[22] Instituto de Astrofísica e Ciências do Espaço, Universidade de Lisboa - OAL, Tapada da Ajuda, 1349-018, Lisboa, Portugal
[23] Kavli Institute for Cosmology, University of Cambridge, Madingley Road, Cambridge, UK
Received 2025 September 11; revised 2025 November 12; accepted 2025 November 20; published 2025 December 16

Abstract

Recent discoveries of dust and molecular gas in quiescent galaxies (QGs) up to $z \sim 4$ challenge the long-standing view that the interstellar medium depletes rapidly once star formation ceases, raising key questions of whether dust and gas coevolve in QGs, and how their depletion links to stellar aging. We present deep Atacama Large Millimeter/submillimeter Array Band 6 continuum and CO(3–2) observations of 17 QGs at $z \sim 0.4$ in the COSMOS field. Using the dust-to-molecular gas mass ratio ($\delta_{\rm DGR}$) as a key diagnostic, we trace postquenching evolution of the cold interstellar medium. Our study triples the number of QGs with direct $\delta_{\rm DGR}$ estimates, constraining 12 systems with stellar population ages of ∼5–10 Gyr. For the first time, we show that $\delta_{\rm DGR}$ in QGs ranges from ∼8× below to ∼2.5× above the canonical value of $\delta_{\rm DGR} \sim 1/100$. Despite uniformly low molecular gas fractions (median $f_{\rm H_2} = M_{\rm H_2}/M_\star \sim 4.1\%$), QGs follow diverse evolutionary paths: about half exhibit rapid (∼700 Myr) exponential dust decline with age, while the rest show mild decline over $\gtrsim$2 Gyr, maintaining elevated $\delta_{\rm DGR} \gtrsim 1/100$. Our results support simulations' predictions of dust and molecular gas evolving independently postquenching, without a preferred quenching mode. This challenges the use of dust continuum as a H_2 tracer, implying that quenching cannot be robustly linked to interstellar medium conditions when relying solely on dust or gas.

Unified Astronomy Thesaurus concepts: Galaxy evolution (594); Interstellar dust (836); Interstellar molecules (849)

1. Introduction

Quiescent galaxies (QGs) are known to host little to no star formation, as quenching processes transform their interstellar medium (ISM), suppressing stellar activity. While their stellar component has been extensively studied out to $z \sim 7$ (A. Weibel et al. 2025), its connection to quenching and late-stage cold ISM evolution remains poorly understood. The long-standing paradigm of QGs being deprived of cold ISM is now challenged by growing evidence of significant molecular gas and dust up to $z \sim 4$. These seminal works push the limit of faint ISM detection via stacking (A. W. S. Man et al. 2016, R. Gobat et al. 2018; G. E. Magdis et al. 2021), a few individual Atacama Large Millimeter/submillimeter Array (ALMA) detections (T. Morishita et al. 2022; M. M. Lee et al. 2024; J. S. Spilker et al. 2025), or via reddened attenuation profiles observed with the James Webb Space Telescope (JWST; D. J. Setton et al. 2024; J. C. Siegel et al. 2025).

Interpreting such measurements is challenging because a wide range of methods often compensates for the lack of individual detections. Estimates of cold molecular gas masses ($M_{\rm H_2}$) make use of CO and [C II] signatures, and are mostly biased to recently quenched or ultramassive systems (S. Belli et al. 2021; C. C. Williams et al. 2021; R. Bezanson et al.

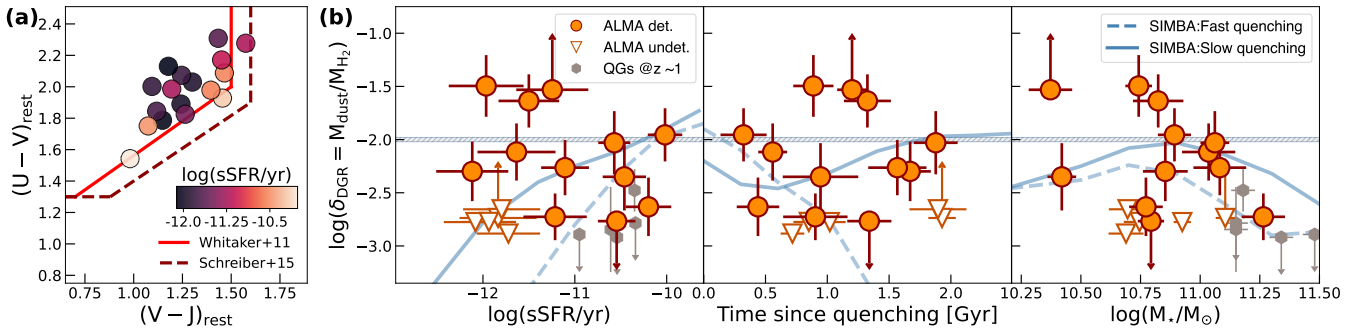

Figure 1. (a) Selected QGs in the UVJ plane, color-coded by sSFR. (b) Evolution of $\delta_{\rm DGR}$ with sSFR, $t_{\rm q}$, and $M_\star$. Large circles mark QGs detected with ALMA (10 in both CO and dust, 1 in either CO or dust); triangles show nondetections in both CO and Band 6 dust continuum. Small points are literature QGs at $z\sim1$ (J. S. Spilker et al. 2025). For all symbols, the lower or upper limits of $\delta_{\rm DGR}$ are denoted with arrows. Solid lines show fast and slow quenching tracks for $z\sim0.4$ QGs from SIMBA (G. Lorenzon et al. 2025). The horizontal line marks the canonical $\delta_{\rm DGR}\sim1/100$.

2022; P.-F. Wu et al. 2023; A. Zanella et al. 2023; K. A. Suess et al. 2025; H. Umehata et al. 2025). For more evolved QGs, such constraints are rare (J. Spilker et al. 2018), and typically rely on the use of dust continuum (D. Donevski et al. 2023) from stacking (R. Gobat et al. 2018; G. E. Magdis et al. 2021; D. Blánquez-Sesé et al. 2023; S. Adscheid et al. 2025), since individual ALMA dust continuum detections are limited to only a handful of QGs at $z\sim1$–4 (C. Schreiber et al. 2018; K. E. Whitaker et al. 2021b; T. Morishita et al. 2022; M. M. Lee et al. 2024; S. D. Stevenson et al. 2025).

Even when detected, dust traces $M_{\rm H_2}$ only via assumed dust-to-gas ratio ($\delta_{\rm DGR}={\rm M_{dust}/M_{gas}}\sim1/100$), calibrated on star-forming galaxies (SFGs; G. E. Magdis et al. 2012; N. Scoville et al. 2016) and often treated as redshift independent (G. Popping et al. 2023). Using this canonical conversion yields uncertain dust-based H_2 fractions (∼1%–20%; R. Gobat et al. 2022). Together with the limitations of stacking, this challenges our understanding of processes acting on the cold ISM in individual QGs.

Similar disagreement arises in interpreting the dust fraction ($f_{\rm dust}=M_{\rm dust}/M_\star$) for which early dust studies find a strong anticorrelation with stellar population age, suggesting rapid dust removal within ∼150–250 Myr (e.g., Z. Li et al. 2019), mirroring a fast H_2 depletion during quenching (K. E. Whitaker et al. 2021b). However, this uniform picture has been questioned by works pointing to possible dust reformation in QGs (D. Donevski et al. 2023) and longer removal timescales (>1–2 Gyr; M. M. Lee et al. 2024; M. J. Michałowski et al. 2024). Theoretical studies based on SIMBA cosmological simulation (R. Davé et al. 2019) further suggest a complex interplay of molecular gas and dust, producing a broad range of $\delta_{\rm DGR}$ in QGs (K. E. Whitaker et al. 2021a; G. Lorenzon et al. 2025). Whether this diversity reflects true physical complexity or stems from methodological biases in probing ISM in QGs remains an open question (R. Gobat et al. 2022).

Disentangling the impact of quenching pathways from ISM evolution in QGs requires direct, independent measurements of both dust and gas masses, i.e., their $\delta_{\rm DGR}$. Efforts so far have focused on high-z, where SFGs show an increase in ISM content from $z\sim0$ to $z\sim2$ (L. J. Tacconi et al. 2018), a trend QGs may share (G. E. Magdis et al. 2021). A first systematic study of five QGs at $z\sim1$ reported low but diverse values ($\delta_{\rm DGR}<1/300-1/1200$; J. S. Spilker et al. 2025). However, the limited sample size and bias toward the most massive and H_2-rich QGs leave open the key question of whether molecular gas and dust evolve similarly after quenching, and whether this evolution is solely driven by their stellar properties, such as age and mass.

In this Letter, we present deep ALMA observations of 17 homogeneously selected QGs at $z\sim0.4$, simultaneously probing their cold dust and molecular gas. By jointly measuring dust and H_2 masses, we aim to provide the first unbiased view of their coevolution in the late phases of galaxy evolution. Throughout the Letter, we assume a Planck Collaboration et al. (2020) cosmology.

2. Observations of Molecular Gas and Dust in QGs

2.1. Targets

Our ALMA Band 6 observations target 17 QGs in the COSMOS field drawn from a statistical parent sample of ∼500 QGs combining deep, medium resolution spectroscopy (hCOSMOS; I. Damjanov et al. 2018) with >15 photometric bands from homogeneously calibrated catalogs (HELP; R. Shirley et al. 2019). We refer to D. Donevski et al. 2023 (hereafter D23) for a detailed description of the sample. The 17 targeted QGs are selected to lie within a narrow redshift range ($0.33<z<0.43$; median of $z=0.36$),[24] and to be old (stellar population ages >3–10 Gyr) and massive ($10.4<\log(M_\star/M_\odot)<11.25$). The galaxies are required to simultaneously satisfy multiple criteria for quiescence: prominent 4000 Å break ($D_{\rm n}4000>1.5$), no H_β detection from deep optical spectroscopy, and low specific star formation rate (sSFR), >0.6 dex below the J. S. Speagle et al. (2014) main sequence. All targets also satisfy the U-V versus V-J color-color criteria for quiescence (C. Schreiber et al. 2015; see Figure 1(a)). Among them, 11/17 show tentative (∼2σ–3σ) detections in deblended, low-resolution Herschel PACS and/or SPIRE maps (D23), while the remaining 6 yield nondetections.

2.2. ALMA Band 6 Observations, Data Reduction, and Analysis

We use data from ALMA project 2024.1.00814.S (PI: Lorenzon), obtained in multiple observing sessions between 2024 October 4 and December 1 (Cycle 11). Observations were conducted with the 12 m array in the C-3 configuration, with varying on-source integration time (30–95 minutes) totaling 26.4 hr. Band 6 was used to cover both the CO(3–2) line transition ($\nu_{\rm rest}=345.796$ GHz) and the dust continuum.

[24] This minimizes redshift-driven variation in H_2 mass evolution.

Integration times were set to reach a signal-to-noise ratio $\geqslant$5 at continuum. For the six PACS/SPIRE-undetected targets, CO emission instead set the limiting factor, assuming likely undetection even with deeper exposures and resulting in $\sim$2$\times$ higher noise levels.

We use CASA (J. P. McMullin et al. 2007) version 6.6.1.17 for both calibration (pipeline 2024.1.0.8) and imaging, conducted with the tclean task with per-source optimization. Continuum maps were extracted with multifrequency synthesis on spectral windows with no line features. Continuum-subtracted spectral cubes on the image plane were used to produce CO moment-zero maps. In both procedures, we use a natural weighting scheme to maximize the recovery of large faint structures. We opted for untapered images to avoid contamination from nearby bright sources (4/17 cases; Figure 8 in Appendix D) and to keep flux extraction homogeneous, having verified that a heavy taper (2″) raises the measured continuum fluxes of <10%. The resulting beam sizes of $\sim$0.″8–0.″9 allow for resolving most sources over 3–4 beams. We reach deep background levels of rms = 9–15 μJy beam^{-1} in the continuum and 7–20 mJy beam^{-1} km s^{-1} for the CO line. Fluxes are extracted using Photutils (L. Bradley et al. 2024) Kron apertures, selecting regions above 2$\times$ rms, and applying deblending in the case of close continuum emissions. Out of 17 targets, 10 show >3σ detections in both dust and CO(3–2), 1 only in continuum, and 1 only in CO (see Figure 8). Among the remaining five QGs undetected with ALMA in both tracers, four lack archival IR data, while one has Spitzer MIPS and PACS 100 μm fluxes. Thus, both ALMA-detected and ALMA-undetected QGs include cases with and without archival IR detections.

Overall, our sample provides the largest dataset of QGs with joint dust and H_2 measurements, tripling known samples beyond the local Universe. We stack the five ALMA-undetected QGs but find no signal, with 1σ sensitivities reaching 5 μJy for dust continuum, and 10 mJy beam^{-1} km s^{-1} for CO(3–2).

2.3. Physical Properties

To estimate the physical properties of QGs, we use the v2025 CIGALE code (M. Boquien et al. 2019) and perform spectral energy distribution (SED) fitting following the methodology from D23. An extended description of our SED fitting is provided in Appendix A. Briefly, we model the stellar emission using G. Bruzual & S. Charlot (2003). We apply a flexible star formation history (SFH) combining delayed and quenched components, and a two-component attenuation law with age-dependent reddening (S. Charlot & S. M. Fall 2000). For dust emission, we employ B. T. Draine & A. Li (2007) library. Our dataset has broad optical-to-near-infrared (NIR) coverage (15+ bands) and up to 5 mid-IR to submillimeter points (detections or upper limits) from D23, supplemented with our ALMA data and, when available, JWST NIRCam (14/17 sources) and MIRI (9/17 sources) fluxes (M. Shuntov et al. 2025). We adopt as our fiducial $M_{\rm dust}$ the values derived from the CIGALE fits. Recent theoretical works have shown that, because dust SEDs of QGs are often constrained by only a single measurement on the Rayleigh–Jeans tail, $T_{\rm dust}$ can be overestimated and, consequently, $M_{\rm dust}$ underestimated (R. K. Cochrane et al. 2022). To evaluate this potential bias, we also derive $M_{\rm dust}$ with alternative approaches that adopt different $T_{\rm dust}$, and find consistent results (see Appendix B).

We infer $M_{\rm H_2}$ by using velocity-integrated fluxes from the moment-zero map and applying the standard procedure (P. M. Solomon & P. A. Vanden Bout 2005). We assume a line ratio of $R_{31} = L'_{\rm CO}(3-2)/L'_{\rm CO}(1-0) = 0.5$, and a constant conversion factor $\alpha_{\rm CO} = 4.36\,M_\odot$(K km s^{-1}pc^{-2}) consistent with similar works (e.g., A. Smercina et al. 2022, H. Umehata et al. 2025). This choice also follows J. S. Spilker et al. 2025, who compared different dust (or gas) detected QGs and is in line with a nonevolving $\alpha_{\rm CO}$ for metal-rich systems across different redshifts and dust luminosities (L. Dunne et al. 2022). As in the aforementioned works, we explore the effect of systematic uncertainties propagated by the unconstrained R_{31} and $\alpha_{\rm CO}$ (Appendix D). We perform this check first by propagating uncertainties on the derivation of $\delta_{\rm DGR}$ and then by constraining the overall sample scatter via a novel use of the Hierarchical Monte Carlo Method.

Together, this allows us to directly constrain $\delta_{\rm DGR}$ for the 10 QGs detected in both CO and dust, and to set lower and upper limits for the CO-only and dust-only detections, respectively. For the ALMA-undetected source with archival IR data, we combine its Spitzer/MIPS and PACS 100 μm fluxes with our 1 mm flux upper limit to estimate $M_{\rm dust}$ and thus an upper limit on $\delta_{\rm DGR}$. For the remaining four ALMA nondetections, throughout the Letter, we show $\delta_{\rm DGR}$ resulting from continuum and CO upper limits.[25] The sources and their derived properties are summarized in Appendix D and Table 1.

3. Direct Probe of $\delta_{\rm DGR}$ in Old QGs

With our sample, we directly access $\delta_{\rm DGR}$, which quantifies the fraction of the ISM mass in dust grains (G. Popping et al. 2023). In Figure 1(b), we illustrate a striking diversity in $\delta_{\rm DGR}$ across stellar properties, namely sSFR, time since quenching ($t_{\rm q}$; defined as a lookback time to the truncation of star formation), and stellar mass ($M_\star$). The variation in $\delta_{\rm DGR}$ exceeds 1 order of magnitude, even excluding ALMA-undetected QGs. This large spread ($\delta_{\rm DGR} \sim 1/700$ to $1/40$) deviates by $\sim$8$\times$ below and $\sim$2.5$\times$ above the canonical value of $\delta_{\rm DGR} \sim 1/100$, regardless of how $M_{\rm dust}$ and $M_{\rm H_2}$ are estimated (see Appendix B). This marks the first direct confirmation that $\delta_{\rm DGR}$ in QGs can exceed values typical for SFGs.

The broad range of $\delta_{\rm DGR}$ suggests that QGs contain complex ISM despite their low sSFR. Notably, the left and mid-panels of Figure 1(b) reveal that the highest $\delta_{\rm DGR}$ arises at low sSFRs, $\gtrsim$1 Gyr postquenching, weakening the link to residual star formation. Interestingly, the presence of similarly massive, dust-attenuated QGs persisting for >1 Gyr after quenching has recently been independently revealed by MIRI observations (K. Lisiecki et al. 2025). Although we do not see a strong anticorrelation with stellar mass, QGs with $\delta_{\rm DGR} \gtrsim 1/100$ are restricted to $M_\star < 10^{11}\,M_\odot$. This supports results from dust stacking studies at high-z (D. Blánquez-Sesé et al. 2023) and the idea that the most massive QGs limit $\delta_{\rm DGR}$ due to efficient dust destruction or heating in massive halos (Y. Zheng et al. 2022; G. Lorenzon et al. 2025; J. S. Spilker et al. 2025). Similar arguments apply to massive lensed QGs at $z \gtrsim$ 1-2 (C. C. Williams et al. 2021; K. E. Whitaker et al. 2021b), where continuum nondetections likely reflect rapid dust removal or destruction rather than insufficient ALMA depth.

In Figure 1(b), we show SIMBA simulation tracks for rapid and slow quenching modes, separated at a quenching time of

[25] These are not listed in Table 1 due to the lack of firm constraints.

$t_q \sim 2 \times 10^8$ yr (G. Lorenzon et al. 2025).[26] These modes broadly (but not exclusively) reflect feedback efficiencies from active galactic nuclei (AGN), with long-term gas heating contributing postquenching. Our QGs span a wide range of t_q, suggesting influence from multiple quenching channels (e.g., S. Belli et al. 2021; M. Park et al. 2023). As seen in Figure 1(b), both ALMA-detected and undetected QGs do not align cleanly with fast or slow quenching tracks. This suggests that ISM and stellar properties in QGs are not solely determined by quenching mode but by a more complex interplay (G. Lorenzon et al. 2025). The QGs with larger δ_{DGR}, however, are broadly consistent with slow quenching, often lying above modeled tracks, suggesting that dusty QGs may be common among slowly quenching, intermediate-mass systems ($M_\star < 10^{11} M_\odot$; G. Lorenzon et al. 2025). Because t_q comes from the CIGALE best-fit SFH, it is sensitive to the SFH parameterization. To assess the robustness of our fiducial estimates, we repeat the analysis using a smoother SFH model (see Appendix D). We find that t_q can vary by up to ∼500 Myr, both below and above the fiducial value, with a tendency toward larger values. The associated δ_{DGR} remains stable, shifting within the errors, confirming that our SFH choice does not affect the results shown in Figure 1(b).

In SFGs, δ_{DGR} variations are often linked to gas-metallicity (e.g., P. De Vis et al. 2019), but this is unlikely for old QGs, which occupy a narrow gas-phase metallicity range (e.g., F. Pistis et al. 2024). We note that δ_{DGR} in this study concerns H_2 gas, ignoring atomic HI. Known studies on early-type galaxies and QGs in the local Universe confirm they can host significant H I reservoirs (up to $\gtrsim 10^{10} M_\odot$; M. J. Michałowski et al. 2024, S. Ellison et al. 2025). However, none of our QGs is individually detected in the MeerKAT-HI survey data with a mass limit down to $\sim 5 \times 10^9 M_\odot$ (A. Bianchetti et al. 2025). Applying our observational selection criteria in SIMBA, we find only $13.05\% \pm 1.08\%$ of QGs above this mass limit. Furthermore, studies at $z \sim 0$ reveal a decrease in the H I-detection fraction toward massive QGs ($\log(M_\star/M_\odot) \gtrsim 10.5$; i.e., H. Guo et al. 2021, S. Ellison et al. 2025). We thus find it unlikely that our QGs are exceptionally H I-rich, and assume that the spread in δ_{DGR} rather reflects diverse timescales for dust and H_2 gas evolution, which we explore in the following sections.

3.1. Evolution of Dust and H_2 Gas Fraction with Stellar Population Age

To explore the drivers of δ_{DGR} variations in our QGs, we examine the age evolution of dust fraction ($f_{dust} = M_{dust}/M_\star$) and gas fraction ($f_{H_2} = M_{H_2}/M_\star$). Our sample contains old systems (mass-weighted ages $\gtrsim$3 Gyr), minimizing contamination from recently quenched objects. Combining it with the depth of our ALMA, we can access previously unexplored regions of the f_{dust}–age plane in old QGs (>5–10 Gyr), providing new constraints on dust depletion timescales.

We probe models with exponential decline ($Ae^{-t/\tau_{dust}}$), adopting short ($\tau_{dust} \sim 0.7$ Gyr) and long ($\tau_{dust} \sim 2$ Gyr) removal timescales normalized to the typical f_{dust} of main-sequence SFGs at $z < 1$ (D. Donevski et al. 2020). These timescales reflect distinct postquenching evolutionary paths

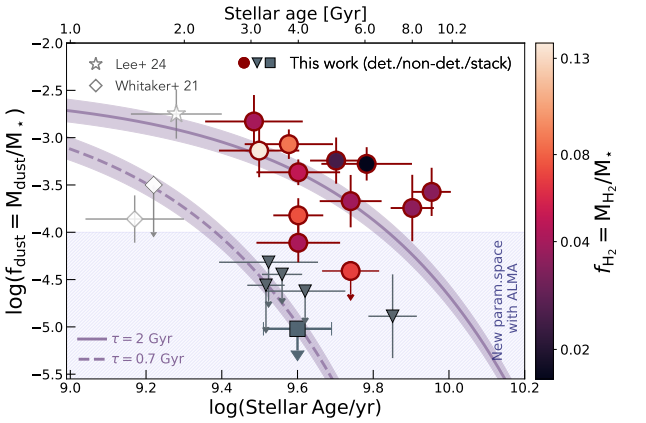

Figure 2. Relation between f_{dust} and mass-weighted stellar age, color-coded by H_2 fraction. As in Figure 1, circles and triangles mark ALMA-detected and nondetected QGs, respectively, with arrows denoting upper limits. The single triangle with an f_{dust} constraint corresponds to a PACS-detected but ALMA-undetected QG. The gray square shows the stacked nondetections in Band 6 dust continuum. Curves trace exponential tracks for fast and slow dust removal from G. Lorenzon et al. (2025). White symbols indicate literature QGs at $z \sim 2$. The shaded region highlights the previously unexplored f_{dust}–age space of old QGs.

found in SIMBA (G. Lorenzon et al. 2025), with shorter τ_{dust} corresponding to efficient dust destruction via thermal sputtering and heating, typically AGN-driven (i.e., H. Hirashita & T. Nozawa 2017). Notably, our QGs, as well as dust-studied ones at $z \sim 2$ (K. E. Whitaker et al. 2021b; M. M. Lee et al. 2024), do not align with a single track in f_{dust} with age (Figure 2), imposing diverse dust depletion (or removal) timescales. In low-redshift poststarbursts, most studies report an anticorrelation between dust content and stellar age, finding that both dust and gas decline on similar timescales (e.g., $\lesssim$400 Myr; K. D. French et al. 2018; Z. Li et al. 2019; R. Bezanson et al. 2022). Our study extends this investigation to much later evolutionary phases, well beyond the last star formation episode, as ensured by mean $D_n4000 = 1.7$. Despite this difference, H_2 fractions of our QGs are comparable to the limits of such poststarburst measurements and suggest longer depletion timescales, in line with theoretical predictions (G. Lorenzon et al. 2025) and with color-selected early-type galaxies from M. J. Michałowski et al. (2024). Differing from such studies, our results show instead that an increase in f_{dust} at fixed stellar age is not fully mirrored by f_{H_2}. Sustained high f_{dust} toward older ages in gas-poor QGs seems incompatible with passive, age-driven depletion. Longer dust depletion timescales may arise if dust grains are sufficiently large to slow destruction by sputtering, as shown by A. Nanni et al. (2025) and with SIMBA in G. Lorenzon et al. (2025), which invoke replenishment either via minor mergers or internally, via regrowth on metals over $\lesssim$150 Myr timescales, flattening the f_{dust}–age evolution. Therefore, our findings support the SIMBA prediction that, *for at least some ISM-rich QGs*, dust and cold gas may follow divergent paths after quenching.

3.2. Tracing QGs Postquenching Routes with H_2

By reaching low H_2 fractions of $f_{H_2} \lesssim 4\%$ in individual, unlensed QGs (Figure 3), we open a new window onto the lowest levels of residual gas, allowing us to reassess how well f_{H_2} traces the final stages of galaxy evolution. The CO-detected QGs have $1.7\% \lesssim f_{H_2} \lesssim 14\%$ (median $4.1^{+1.2}_{-0.9}\%$), reaching

[26] This cut was found in G. Lorenzon et al. (2025) as a broad separation between the two peaks of the normalized quenching time distribution (see also F. Rodríguez Montero et al. 2019 and Y. Zheng et al. 2022). The redshift-dependent cut is applied here to $z = 0.36$.

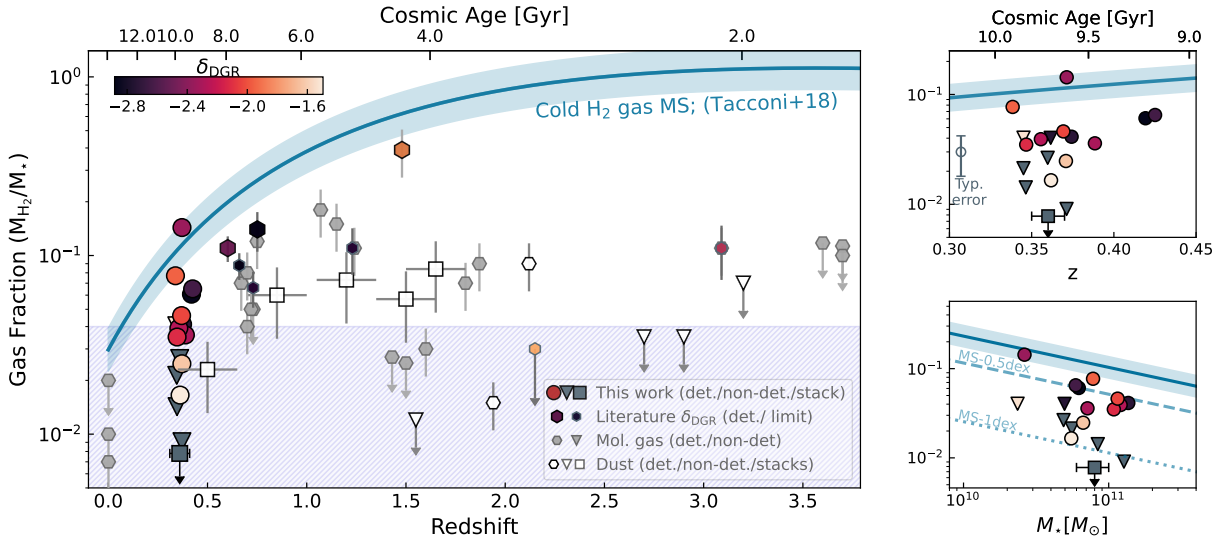

Figure 3. H_2 gas fraction versus redshift for our sample and literature QGs, with detectability (CO- or dust-based) noted in the legend. The points include QGs at $z \sim 1$ (S. Belli et al. 2021; R. Bezanson et al. 2022; C. Woodrum et al. 2022), $z \sim 2$–3 (K. E. Whitaker et al. 2021b; C. C. Williams et al. 2021; T. Morishita et al. 2022; T. L. Suzuki et al. 2022; H. Umehata et al. 2025), and stacks (G. E. Magdis et al. 2021, D. Blánquez-Sesé et al. 2023). Colored symbols show δ_{DGR}, directly estimated only for our sample, two QGs at $z \sim 0.7$ (J. S. Spilker et al. 2025) and a QG at $z \sim 1.5$ (M. Hayashi et al. 2018), with others showing limits. The main-sequence H_2-scaling relation (L. J. Tacconi et al. 2018) is shown in blue. The shaded area shows the new parameter space of f_{H_2} opened for individual detections. The right panel zooms in on our QGs relative to the main-sequence relation at their z and $M_\star$. The typical error on f_{H_2} for our QGs is shown in the upper right subpanel.

0.6% in stacked nondetections. These uniformly low H_2 place our QGs 4–10× below the main-sequence H_2 scaling of L. J. Tacconi et al. (2018), consistent with offsets seen in QGs at $z \sim 1$ (C. C. Williams et al. 2021; C. Woodrum et al. 2022; K. A. Suess et al. 2025). Our estimates of f_{H_2} extend the study of molecular gas properties to older ages with respect to other QGs studies, both at lower (L. M. Young et al. 2011, A. Leśniewska et al. 2023, M. J. Michałowski et al. 2024) and higher redshifts (K. A. Suess et al. 2017), pushing measurements ∼1 dex below detection limits for QGs at the same redshift.

The theoretical suggestion that CO-detected QGs can arise from both slow and fast quenching modes (as shown in Figure 1) is empirically supported by their gas depletion timescales ($\tau_{dep} \propto M_{H_2}/SFR$). Combining M_{H_2} with SED-based SFRs yields τ_{dep} from 0.4 to 48 Gyr. We find recently quenched QGs ($t_q < 1$ Gyr) with shorter τ_{dep} (∼0.4–0.8 Gyr) than older QGs, which average around $\tau_{dep} \sim 10$ Gyr, longer than their t_q. Such older QGs are consistent with inefficient star formation and quenching via slow suppression rather than gas expulsion, resembling the population of slowly quenched old QGs found to have relatively long depletion times in SIMBA (G. Lorenzon et al. 2025). In the simulation, this population is associated with less effective AGN feedback and may require additional gas removal to fully quench. A similar conclusion is reached for older quenched objects at $z \sim 0.7$ (K. A. Suess et al. 2017), where f_{H_2} is comparable to our sample and has been interpreted as evidence for possible morphological quenching. This further aligns with findings for $z \sim 1$ QGs, where diverse pathways imply H_2 depletion alone cannot explain quenching (e.g., S. Belli et al. 2021; P.-F. Wu et al. 2023).

The f_{H_2} evolution diverges not only from the stellar component but also from dust, as Figure 3 shows no clear correlation with δ_{DGR} across $M_\star$. We find a dispersion of ∼0.8 dex (∼1.4 dex with stacked QGs) in f_{H_2}, smaller than ∼1.3 dex (up to ∼2 dex including stacks) in f_{dust} for the same sample (Section 3.1). This indicates that variations in dust content dominate the scatter in δ_{DGR} at fixed $M_\star$. Strikingly, Figure 3 unveils that in the newly accessed regime of very low H_2 fractions, two QGs emerge with $\log \delta_{DGR} \gtrsim -2$, enhanced above typical SFG values. Our most massive QGs ($>10^{11}\,M_\odot$) remain relatively gas-rich, ∼5× below the SFG gas-scaling from L. J. Tacconi et al. (2018), but all exhibit $\delta_{DGR} \lesssim 1/100$, falling below the standard value. This aligns with results from J. S. Spilker et al. (2025), whose two $z \sim 1$ QGs have low $\delta_{DGR} = 1/300$ and $1/750$.

In SIMBA, most QGs of $\log(M_\star/M_\odot) > 10.8$ undergo fast AGN-driven quenching (Y. Zheng et al. 2022), but whether this leads to full ISM removal depends on the balance between multiple processes acting on gas and dust (i.e., dust regrowth; D23). The high-z QGs, small color-coded symbols in Figure 3, illustrate this complexity: the $z \sim 2$ QG from T. Morishita et al. (2022) has a lower limit of $\delta_{DGR} \gtrsim 1/60$ despite AGN outflow and lack of H_2 gas;[27] conversely, the dust-undetected but H_2-rich QGs from H. Umehata et al. (2025) and J. S. Spilker et al. (2025) contain suppressed $\delta_{DGR} \lesssim 1/500$–$1/1000$. Only $z \sim 1.5$ QG (M. Hayashi et al. 2018) shows typical δ_{DGR}, but it is a distant, cool-core cluster object, likely an outlier to the general QG population. These cases suggest two key implications: (1) dust is an unreliable tracer of H_2 mass in QGs; (2) nonuniform ISM evolution in the quenched phase may be common for QGs across redshifts, not merely an artifact of observational methods. This challenges the idea that quenching mode is the sole driver of ISM diversity, supporting models where feedbacks and dust reformation jointly shape the late ISM fate (H. Hirashita & T. Nozawa 2017; G. Lorenzon et al. 2025).

We further explore quenching modes and postquenching evolution in two accompanying works: one provides an in-depth analysis of the gas and stellar structure and kinematics in a few extreme cases driving the δ_{DGR} spread (D. Donevski

[27] This results from the nondetection of [CI]$^3P_2 \rightarrow {}^3P_1$ line emission.

et al. 2025, in preparation), while the other provides a statistical treatment accounting for morphological diversity and AGN radio signatures in our QGs, and characterizes their impact on dust-gas evolution (G. Lorenzon et al. 2025, in preparation).

4. Conclusions

We present the first statistical sample of 17 massive QGs at $z \sim 0.4$, probing their ISM with ALMA Band 6 dust continuum and CO(3–2) emission. For 12/17 systems, we constrain key diagnostics ($\delta_{\rm DGR}$, $f_{\rm dust}$, and $f_{\rm H_2}$) and link them to stellar properties, finding that:

1. Dust-to-gas ratios in QGs span $\delta_{\rm DGR} \sim 1/700$–$1/40$, departing $\sim 8\times$ below to $\sim 2.5\times$ above the canonical value of $\delta_{\rm DGR} \sim 1/100$. Although most QGs align with slow-quenching mode tracks, diverse ISM across stellar mass, age, sSFR, and quenching timescale imply that quenching mode alone cannot explain the observed scatter.
2. The relation between dust fraction and stellar population age shows that some QGs undergo rapid dust decline (within $\tau \sim 0.7$ Gyr), while others retain stable values ($\log f_{\rm dust} \gtrsim -3.5$) even toward the old ages (>6–10 Gyr) and >1 Gyr after quenching, supporting scenarios where dust reformation shapes the late ISM.
3. QGs show no clear relation between molecular gas and dust content across stellar mass, calling into question the reliability of dust as an H_2 tracer.
4. Despite uniformly low H_2 fraction (median $f_{\rm H_2} \sim 4.1^{+1.2}_{-0.9}\%$), the nonmonotonic behavior of $f_{\rm H_2}$, $f_{\rm dust}$, and stellar properties reveals diverse postquenching pathways in QGs. Combined with $z \sim 1$–3 studies, this suggests that cold ISM evolves through mechanisms beyond a simple decline of star-forming conditions.

Our study underscores the challenge of linking quenching modes to postquenching ISM conditions, even with ALMA CO and dust detections. It motivates future model refinements to account for processes that decouple gas and dust to properly simulate ISM in QGs. To this end, a new parameter space of $f_{\rm H_2} < 4\%$ opened for individual QGs highlights the need for JWST+ALMA studies of resolved ISM in QGs across cosmic time.

Acknowledgments

G.L. and D.D. acknowledge support from the NCN SONATA grant (UMO-2020/39/D/ST9/00720). D.D. acknowledges support from the Polish National Agency for Academic Exchange (Bekker grant BPN/BEK/2024/1/00029/DEC/1). A.W.S.M. acknowledges the support of the Natural Sciences and Engineering Research Council of Canada (NSERC) via grant reference No. RGPIN-2021-03046. S.B. is supported by ERC grant 101076080. J. is funded by the European Union (MSCA EDUCADO, GA 101119830 and WIDERA ExGal-Twin, GA 101158446). A.N. and P.S. acknowledge support from the Narodowe Centrum Nauki (UMO2020/38/E/ST9/00077). This Letter makes use of the following ALMA data: ADS/JAO.ALMA#2024.1.00814.S. ALMA is a partnership of ESO (representing its member states), NSF (USA) and NINS (Japan), together with NRC (Canada), NSTC and ASIAA (Taiwan), and KASI (Republic of Korea), in cooperation with the Republic of Chile. The Joint ALMA Observatory is operated by ESO, AUI/NRAO and NAOJ. This research made use of Photutils, an Astropy package for detection and photometry of astronomical sources (L. Bradley et al. 2024). C.P. was supported through DL 57/2016 (P2460) from the "Departamento de Física, Faculdade de Ciências da Universidade de Lisboa." C.P. acknowledges the support by Fundação para a Ciência e a Tecnologia (FCT) through the research grants UIDB/04434/2020 doi:10.54499/UIDB/04434/2020 and UIDP/04434/2020 doi:10.54499/UIDP/04434/2020. I.S. acknowledges fundings from the European Research Council (ERC) DistantDust (grant No. 101117541) and the Atraccíon de Talento grant No. 2022-T1/TIC-20472 of the Comunidad de Madrid, Spain. K.L. acknowledges the support of the National Science Centre, Poland, through the PRELUDIUM grant UMO-2023/49/N/ST9/00746.

Appendix A
Multiwavelength SED Modeling and Fitting of QGs

A.1. SED Fitting Methodology

We use the CIGALE code (M. Boquien et al. 2019), v2025.0, and follow the approach of D23 to estimate the physical properties of our QGs. For the stellar component, we use G. Bruzual & S. Charlot (2003) stellar population synthesis with a G. Chabrier (2003) initial mass function. We sample the stellar metallicity grid points closest to the mass–metallicity relation for each galaxy. We adopt a flexible SFH, modeling a delayed plus quenched component (L. Ciesla et al. 2021), given as

$$\mathrm{SFR} = \begin{cases} t \times e^{-t/\tau_{\rm main}}, & \text{when } t \leqslant t_{\rm trunc} \\ r \times \mathrm{SFR}(t), & \text{when } t > t_{\rm trunc} \end{cases}, \tag{A1}$$

where $\tau_{\rm main}$ is the e-folding time of the main stellar population, while $t_{\rm trunc}$ represents the time at which star formation is truncated, either instantaneously ($r_{\rm SFR} = 0$) or partially ($0 < r_{\rm SFR} < 1$). The parameter r is the ratio between SFRs after quenching and at quenching. We also test nonparametric SFHs by fitting the functional form to the center of the first five age bins, finding results consistent with our fiducial run. We use the S. Charlot & S. M. Fall (2000) double power-law attenuation model with age-dependent differential attenuation between young ($<10^7$ yr) and old stars. For dust SED, we adopt the physically motivated B. T. Draine & A. Li (2007; DL07) library, proven efficient in modeling various galaxy types, including QGs (G. E. Magdis et al. 2021, D. Blánquez-Sesé et al. 2023). We fix the radiation parameter $U_{\rm max} = 10^6$, emission slope ($\beta = 2$), and sample different intensities $U_{\rm min}$. We let the fraction of Polycyclic Aromatic Hydrocarbons (PAHs) vary ($0.47 < q_{\rm PAH} < 4.6$) and limit the illumination fraction γ to 0.01, reducing the chance of overestimating $M_{\rm dust}$. We define $L_{\rm IR}$ as the integral of the SED from 8 to 1000 μm and derive $M_{\rm dust}$ by fitting and normalizing the IR photometry to the DL07 library.

Our dataset includes rich sampling with at least 15 optical-to-NIR bands. At longer wavelengths, it contains our ALMA Band 6 dust continuum fluxes (11 objects) and upper limits (6 objects). Where available, we complement ALMA photometry with mid-IR and/or far-IR fluxes estimated from deblending deep Spitzer MIPS and Herschel PACS/SPIRE maps (D23), and with JWST MIRI fluxes (M. Shuntov et al. 2025). Overall, 11/17 objects resulted in two to four photometric points in the

mid-IR to submillimeter regime, ensuring reliable coverage of the Rayleigh–Jeans tail and proper normalization of the dust SED, key for $M_{\rm dust}$ constraints. In our SED fitting, we exploit the independent prior on $D_{\rm n}4000$ measured from optical spectra. As $D_{\rm n}4000$ is a reliable tracer of stellar age (e.g., I. Damjanov et al. 2018), we use the $D_{\rm n}4000$ option in CIGALE and iterate until measured and SED-derived $D_{\rm n}4000$ agree within ± 0.1. This procedure ensures that modeling correctly matches stellar population ages, reducing dust-age degeneracies. For all physical quantities used throughout this study, we adopt Bayesian (probability-weighted average) values. Quality assessment reveals good fits for all modeled SEDs, with reduced χ^2 ranging from 0.2 to 2.5, and median $\chi^2 = 1.02 \pm 0.33$.

A.2. Stability of SFH

The time at which quenching occurs, $t_{\rm q}$, is sensitive to the assumed SFH, which can in turn bias the inferred stellar properties at the observed epoch. In our fiducial setup, we adopt a standard delayed-τ model, where the SFR is abruptly rescaled at $t < t_{\rm trunc}$. However, such a sharp truncation may not accurately capture the more gradual suppression of star formation. To test smoother quenching scenarios, we construct a custom SFH that extends the standard delayed-τ form by appending an exponential decay term, producing a continuous, slowly declining tail after quenching. We implement this modified SFH as a new module within CIGALE to preserve full self-consistency in our SED fitting framework. Prior to quenching, the SFH follows the canonical delayed functional form:

$$\mathrm{SFR}_{\rm pre}(t) = A\left(\frac{t}{\tau^2_{\rm main}}\right)e^{-t/\tau_{\rm main}}, \quad 0 \leqslant t < t_q \tag{A2}$$

The quenching moment is characterized by a change in the parametrized SFR, enforcing a continuous exponential decline in the form:

$$\mathrm{SFR}_{\rm post}(t) = \mathrm{SFR}_{\rm pre}(t_{\rm q})e^{-(t-t_{\rm q})/\tau_{\rm q}}, \quad t \geqslant t_q, \tag{A3}$$

where τ_q is the new e-folding time during the exponential decline. Using this delayed-exp model of SFH, we find that the inferred stellar mass, mass-weighted stellar age, and sSFR are remarkably stable, with a relative difference per galaxy within 0.2 dex from the fiducial delayed-τ model. This variation is well within the statistical/systematic budgets of our analysis (see Appendix D). A notable difference is instead found for $t_{\rm q}$, which shifts toward larger values for $\sim$70% when the exponential tail is added. This is a natural consequence of the smoother SFR decline, pushing the quenching toward earlier times to maintain the overall old stellar population without a significant impact on the present SED. The increase in quenching time does not affect our conclusions but rather reinforces our interpretation of long-lasting dust reservoirs.

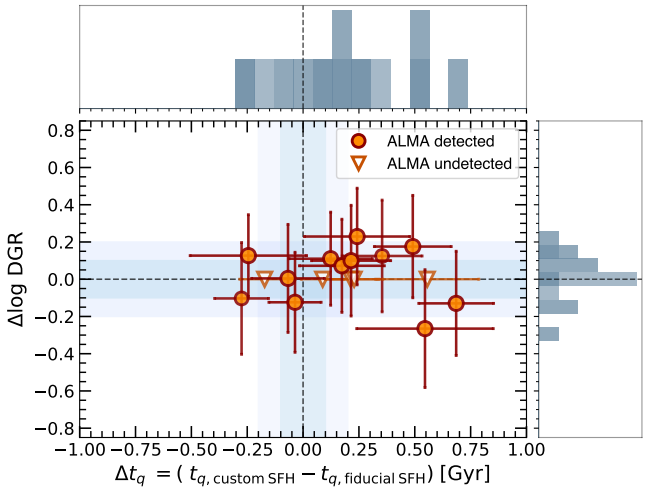

Figure 4. Per-galaxy variation of $\delta_{\rm DGR}$ and time since quenching, adopting a delayed-tau ($t_{\rm q,customSFH}$) and a delayed+exp ($t_{\rm q,fiducialSFH}$) SFH model. Non-detections are shown as empty triangles.

The full variation of the $\delta_{\rm DGR}$ and $t_{\rm q}$ within the different choices of SFH is shown in Figure 4.

A.3. Inspecting SED Fitting Systematics

To assess the robustness of our SED fitting approach and quantify potential biases, we exploit a widely used method (e.g., L. Ciesla et al. 2021) for generating a simulated dataset and analyzing it using the same methodology applied to our observed galaxies. The primary goal is to evaluate how observational effects might influence the recovery of physical parameters through SED modeling. We use the "mock object" functionality within CIGALE to construct a synthetic catalog, leveraging the best-fit SED model of each galaxy in our sample. This creates one artificial object per galaxy, for which the input physical parameters are known by construction. These models are then integrated through the same set of photometric filters as used in the observed data. To simulate observational uncertainties, we perturb the model fluxes by adding Gaussian noise, with σ matching the measured uncertainty in each photometric band. The mock galaxies are then refitted using the same grid of physical models and priors as in the real sample, enabling a direct comparison between the recovered (output) and true (input) parameters.

In Figure 5, we show the residuals between input and output parameters as a function of $M_\star$ and the $D_{\rm n}4000$ index, measured from optical spectra. This test reveals a consistency between input and output values, as recovered trends for all physical parameters (namely, stellar population age, stellar mass, dust mass, and time since quenching) closely follow the one-to-one relation, defined by a small mean offset and low scatter around zero value. In summary, this supports the reliability of the derived physical properties across our QG sample.

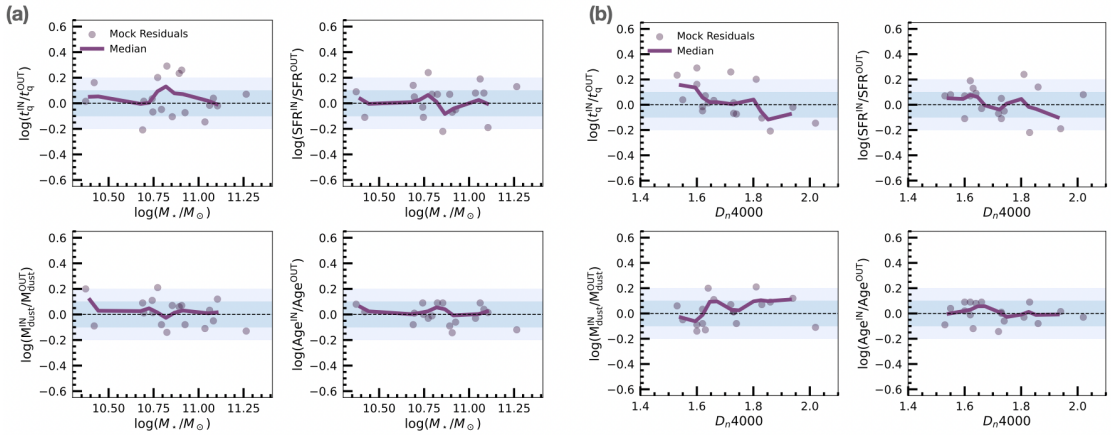

Figure 5. Results of our mock CIGALE analysis quantifying the offset between the mock input ("true") and SED-fitting output ("observed") parameters, as a function of $M_\star$ and independently measured D_n4000. Dark violet lines show binned means, indicating good constraints with no systematic offsets.

Appendix B
Comparison of Different Methods for Deriving $M_{\rm dust}$

In this study, we choose as a fiducial method the physically motivated DL07 dust emission library, and to assess potential systematics in $M_{\rm dust}$ estimates, we compare it with two alternative, commonly used methods. First, we apply a single temperature optically thin modified blackbody model implemented within the CIGALE code. We adopt a fixed dust temperature of $T_{\rm dust} = 21$ K, representative of QGs (G. E. Magdis et al. 2021). We also test the empirical calibration of N. Scoville et al. (2016), which estimates $M_{\rm dust}$ directly from ALMA flux density at rest-frame 850 μm using

$$M_{\rm dust} = \frac{S_{\nu,\rm obs} D_L^2}{\kappa_{\nu_{\rm rest}}(1+z)} \left(B_{\nu_{\rm rest}}(T_{\rm dust})\right)^{-1}, \quad \text{(B1)}$$

where $B_\nu(T)$ is the Planck function evaluated at temperature T, and $\kappa_\nu \equiv \kappa_{\nu_0}(\nu/\nu_0)^\beta$ is the dust absorption coefficient. We adopt the standard emissivity of $\kappa_{\nu_0} = 2.64$ m^2 kg^{-1} at 125 μm (L. Dunne et al. 2011), and assume $\beta = 2.0$, keeping $T_{\rm dust} = 21$ K to be consistent with the literature. We apply both methods to our ALMA-detected QGs and compare the resulting $M_{\rm dust}$, $f_{\rm dust}$, and $\delta_{\rm DGR}$ to our fiducial DL07-based values. As shown in Figure 6, all methods yield values generally consistent within $\sim$0.2 dex. The overall agreement supports the robustness of our estimates, though uncertainties remain due to the assumed $T_{\rm dust}$ and limited knowledge about the AGN presence in our sources.

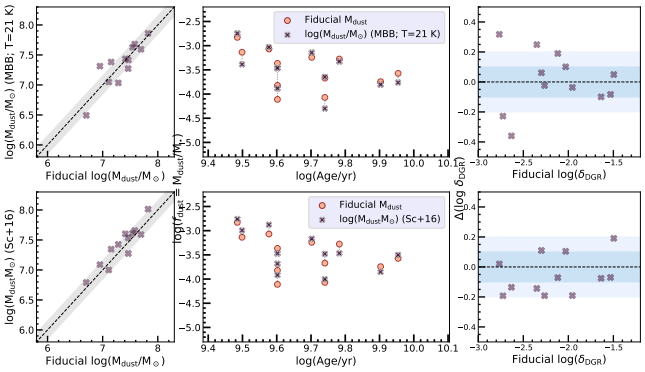

Figure 6. Comparison of fiducial dust properties with alternative dust-mass estimates (upper: versus modified blackbody fits; lower: versus N. Scoville et al. 2016). We consider 12 QGs with direct ALMA estimates. From left to right: comparisons of our fiducial values versus alternative methods to estimate $M_{\rm dust}$, $f_{\rm dust}$, and $\log(\delta_{\rm DGR})$.

Appendix C
Impact of Systematics on CO-to-H_2 Conversion

In this study, we follow the P. M. Solomon & P. A. Vanden Bout (2005) prescription to derive M_{H_2} from the integrated CO(3–2) line flux. We first convert the flux into CO-luminosity $L'_{CO}(3-2)$ in units of K km s^{-1} pc^2 and then convert it into CO(1–0) luminosity $L'_{CO}(1-0)$ through the line ratio $R_{31} = L'_{CO}(3-2)/L'_{CO}(1-0)$. We then convert the luminosity to mass using $M_{H_2} = \alpha_{CO} \times L'_{CO}(1-0)$, where M_{H_2} is in $M_\odot$. The R_{31} and α_{CO} parameters are largely unconstrained for old QGs at intermediate redshift and thus are important sources of systematic errors as explored in J. S. Spilker et al. (2025) and H. Umehata et al. (2025). We quantify the effect of uncalibrated R_{31} and α_{CO} by treating a wide range of their possible values as systematic error and propagating it on the derived $\delta_{\rm DGR}$. We propagate the uncertainties using a Monte Carlo method, recalculating $\delta_{\rm DGR}$ 10,000 times for each galaxy with simultaneous continuum and CO(3–2) detections. In each realization, we resample the fiducial $M_{\rm dust}$, the integrated CO line flux (S_{CO}), and the parameters R_{31} and α_{CO}. We draw each measured quantity from a normal distribution centered on its measured value, with a standard deviation equal to its observational uncertainty. We treat the fiducial $M_{\rm dust}$ as a measured quantity, since the parameter space governing the dust emission modeling has already been extensively explored within CIGALE (see Appendix B). We sample R_{31} from a broad uniform distribution ($0.10 < R_{31} < 0.55$). The adopted range reflects plausible R_{31} values for our QGs, where low CO excitation is expected in the absence of star formation (E. Bayet et al. 2013; Z. Li et al. 2020), which in turn minimizes the derived $\delta_{\rm DGR}$. For α_{CO}, we adopt a log-uniform prior to capture the very broad modeled and observed ranges (D. Narayanan et al. 2012; A. D. Bolatto et al. 2013; M. J. Michałowski et al. 2024), slightly extended to $0.5 < \alpha_{CO} < 5$. The resulting uncertainties on the per-galaxy $\delta_{\rm DGR}$ are calculated as the 16th and 86th percentiles of the per-galaxy $\delta_{\rm DGR}$ distribution and are reported in Figure 7. Systematic uncertainties dominate the propagated measurement

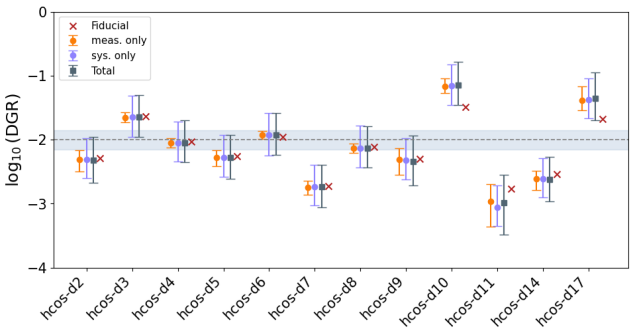

Figure 7. Per-galaxy propagated uncertainties on the $\delta_{\rm DGR}$ accounting for only measurement errors (orange), only $\alpha_{\rm CO}$ and R_{31} systematics (violet), and both (gray). Dots represent the median of the derived per-galaxy $\delta_{\rm DGR}$ distribution, while error bars are the 16th and 86th percentile levels. Red cross markers show the fiducial values adopted in the Letter. The dashed line corresponds to the reference value of $\delta_{\rm DGR} = 1/100$, and the light-blue band represents the 0.15 dex dispersion measured for SFGs (G. E. Magdis et al. 2012).

errors, yet they do not fully account for the observed spread in $\delta_{\rm DGR}$ across the sample. The light-blue bands show the scatter in the G. E. Magdis et al. (2012) relation around the reference value $\delta_{\rm DGR} = 1/100$ for SFGs (as in Figure 1).

To further assess the impact of systematics on $\delta_{\rm DGR}$, we apply a Hierarchical Markov Chain Monte Carlo (HMCMC) analysis that treats the population median and intrinsic scatter as free hyperparameters. In the absence of a predictive model for the molecular gas mass in our galaxies, the HMCMC does not aim to constrain the most probable $\delta_{\rm DGR}$ values from the data, but rather to assess how strongly the adopted priors influence the shape and spread of the posterior distribution. While doing this, the influence of systematic uncertainty on the full-sample spread can be assessed from the distribution of hyperparameters. Using the same prior ranges adopted for the estimation of systematic uncertainties, we obtain as best parameters $R_{31} = 0.35^{+0.10}_{-0.10}$, $\log(\alpha_{\rm CO}) = 0.30^{+0.10}_{-0.10}$, and hyperparameters $\log(\mu_{\rm DGR}) = -1.99^{+0.21}_{-0.22}$ and $\log(\sigma_{\rm DGR}) = -0.68^{+0.25}_{-0.23}$ with values obtained as median of the corresponding parameters/hyperparameters distribution and errors as 16th and 86th percentiles. While the wide errors broadly reflect the overall spread in priors, the hyperparameters describe a relatively stable $\delta_{\rm DGR}$ distribution, with a dispersion $\sim$1 dex larger than the median $\delta_{\rm DGR}$ spread per-galaxy $\log(\sigma_{\rm gal}) = 0.04$. This reinforces the idea that the observed spread of the sample is driven by intrinsic galaxy properties rather than statistical errors.

Appendix D
Properties of ALMA-observed QGs from This Study

We show in Figure 8 the untapered, primary-beam–corrected ALMA Band 6 moment-zero maps of the 17 sources in our sample, together with their corresponding optical counterparts from JWST (or HST when JWST imaging is not available). The optical images illustrate the morphological diversity of the sample, while the ALMA maps highlight the range of submillimeter emission and the differences between

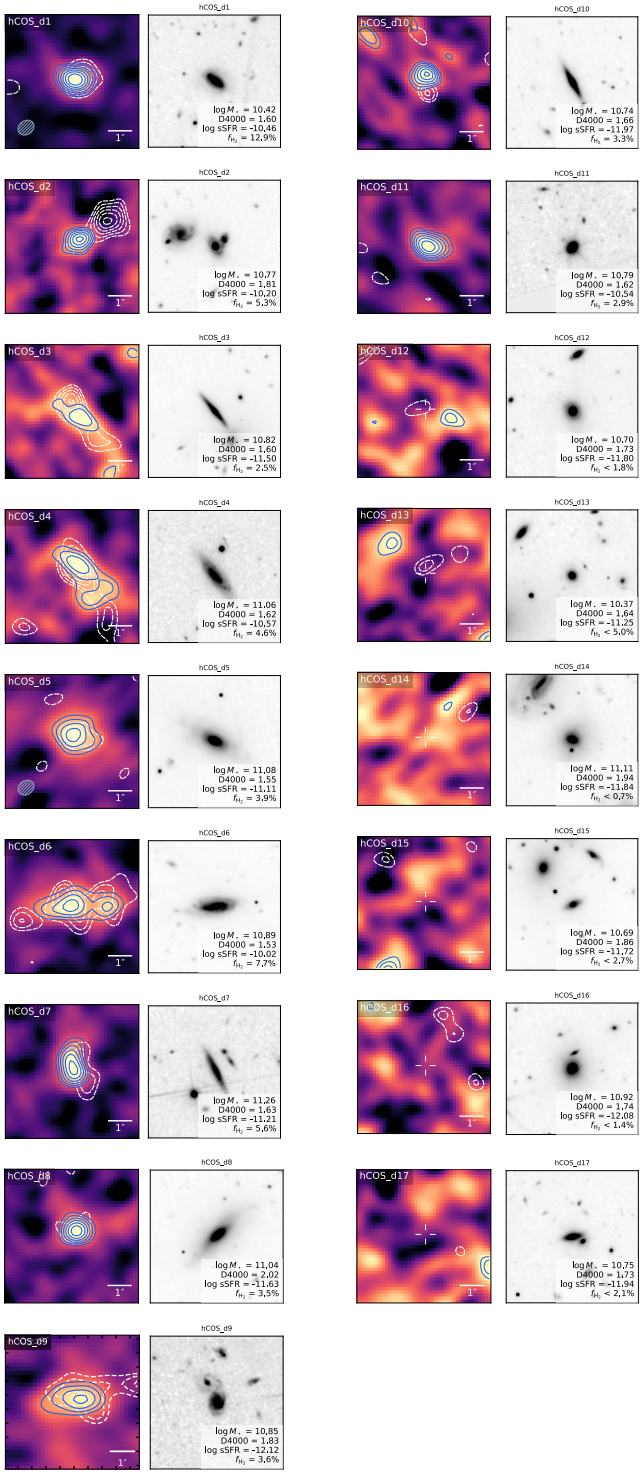

Figure 8. For each QG: left: ALMA Band 6 primary-beam corrected moment-zero map ($5'' \times 5''$ size) overlaid with dust continuum contours (white dashed) and CO(3–2) contours (blue solid) increasing from 2σ with 1σ step. Typical beam size of $0.''85 \times 0.''7$ and $1''$ scale (corresponding to $\sim$5 kpc) are shown; right: stellar emission from JWST F277W (or Hubble Space Telescope F160W for sources hCOS-d7 and hCOS-d9) with basic physical properties annotated in the lower-right corner.

Table 1
Summary of Physical Properties for QGs in This Work

Name	R.A. (deg)	Decl. (deg)	z	$\log(M_\star/M_\odot)$	$\log(\mathrm{Age}_\star/\mathrm{yr})$	$\log(\mathrm{sSFR/yr})$	$S_{1\mathrm{mm}}$ (μJy)	S_{CO} (Jy km/s)	$M_{\mathrm{H_2}}$ ($10^9 M_\odot$)	M_{dust} ($10^7 M_\odot$)	$\log(\delta_{\mathrm{DGR}})$
hCOS-d1	150.350298	2.222278	0.371	10.42	9.62	−10.46	66 ± 11	0.56 ± 0.02	4.29 ± 0.15	1.92 ± 0.29	−2.34
hCOS-d2	150.484972	2.082486	0.425	10.77	9.60	−10.20	30 ± 8	0.39 ± 0.05	3.84 ± 0.24	0.89 ± 0.18	−2.63
hCOS-d3	150.219218	2.059187	0.371	10.82	9.70	−11.50	112 ± 12	0.27 ± 0.04	1.65 ± 0.11	3.82 ± 0.31	−1.64
hCOS-d4	149.956582	1.788010	0.369	11.06	9.60	−10.57	97 ± 15	0.89 ± 0.04	5.31 ± 0.14	4.96 ± 0.39	−2.03
hCOS-d5	149.920863	2.031208	0.356	11.08	9.74	−11.12	104 ± 24	0.85 ± 0.07	4.73 ± 0.36	2.58 ± 0.60	−2.26
hCOS-d6	149.845755	1.974381	0.338	10.89	9.58	−10.02	284 ± 10	1.20 ± 0.03	6.01 ± 0.15	6.66 ± 0.24	−1.96
hCOS-d7	150.602639	2.118054	0.374	11.26	9.60	−11.21	54 ± 11	1.23 ± 0.06	7.59 ± 0.22	1.43 ± 0.29	−2.73
hCOS-d8	150.348257	1.948979	0.347	11.04	9.95	−11.63	91 ± 11	0.72 ± 0.08	3.80 ± 0.18	2.90 ± 0.27	−2.12
hCOS-d9	149.585279	2.557561	0.388	10.85	9.90	−12.12	47 ± 19	0.39 ± 0.06	2.57 ± 0.40	1.29 ± 0.52	−2.30
hCOS-d10	150.386240	2.222691	0.362	10.74	9.56	−11.94	93 ± 8	0.35 ± 0.03	2.41 ± 0.18	5.12 ± 0.21	−1.49
hCOS-d11	149.790964	1.919023	0.419	10.79	9.74	−10.54	<21	0.48 ± 0.04	3.78 ± 0.32	<0.5	<−2.77
hCOS-d12	150.224869	2.236685	0.362	10.70	9.52	−11.80	<42	<0.13	<0.90	<0.50	⋯
hCOS-d13	149.871032	2.233226	0.345	10.37	9.49	−11.25	121 ± 22	< 0.12	<1.18	3.48 ± 0.30	>−1.53
hCOS-d14	150.182112	2.113393	0.371	11.11	9.85	−11.84	<28	<0.13	<0.90	(0.17 ± 0.12)	(>−2.74)
hCOS-d15	150.094894	2.297028	0.360	10.69	9.52	−11.72	<84	<0.2	<1.5	<0.3	⋯
hCOS-d16	150.184392	2.067280	0.346	10.92	9.62	−12.08	<84	<0.2	<1.5	<0.3	⋯
hCOS-d17	149.875440	2.200613	0.345	10.75	9.56	−11.94	<84	<0.2	<1.5	<0.3	⋯

Note. R.A. and decl. correspond to J2000 coordinates; $S_{1\mathrm{mm}}$ is the observed integrated ALMA flux density; S_{CO} is the velocity-integrated line flux; $M_{\mathrm{H_2}}$ is derived assuming $\alpha_{\mathrm{CO}} = 4.36$; $\log(\delta_{\mathrm{DGR}})$ denotes the logarithmic dust-to-gas ratio, defined as $\log(M_{\mathrm{dust}}/M_{\mathrm{mol}})$; values in parentheses correspond to source for which M_{dust} was estimated by fitting the DL07 dust model using available archival photometry from deblended low-resolution Spitzer MIPS and Herschel PACS/SPIRE images, complemented with ALMA upper limits from this study. Given the significant uncertainties associated with this method, these values should be interpreted with caution.

the gas and dust components. The global stellar and interstellar-medium properties of the sample are listed in Table 1.

ORCID iDs

G. Lorenzon https://orcid.org/0009-0002-8726-8917
D. Donevski https://orcid.org/0000-0001-5341-2162
A. W. S. Man https://orcid.org/0000-0003-2475-124X
M. Romano https://orcid.org/0000-0002-9948-3916
K. E. Whitaker https://orcid.org/0000-0001-7160-3632
S. Belli https://orcid.org/0000-0002-5615-6018
D. Liu https://orcid.org/0000-0001-9773-7479
M. M. Lee https://orcid.org/0000-0002-2419-3068
D. Narayanan https://orcid.org/0000-0002-7064-4309
A. Long https://orcid.org/0000-0002-7530-8857
I. Shivaei https://orcid.org/0000-0003-4702-7561
A. Nanni https://orcid.org/0000-0001-6652-1069
K. Lisiecki https://orcid.org/0009-0004-1140-3363
P. Sawant https://orcid.org/0000-0002-0498-8074
G. Rodighiero https://orcid.org/0000-0002-9415-2296
I. Damjanov https://orcid.org/0000-0003-4797-5246
Junais https://orcid.org/0000-0002-7016-4532
R. Davé https://orcid.org/0000-0003-2842-9434
C. Pappalardo https://orcid.org/0000-0003-2606-6019
C. Lovell https://orcid.org/0000-0001-7964-5933
M. Hamed https://orcid.org/0000-0001-9626-9642

References

Adscheid, S., Magnelli, B., Ciesla, L., et al. 2025, A&A, 702, A186
Bayet, E., Bureau, M., Davis, T. A., et al. 2013, MNRAS, 432, 1742
Belli, S., Contursi, A., Genzel, R., et al. 2021, ApJL, 909, L11
Bezanson, R., Spilker, J. S., Suess, K. A., et al. 2022, ApJ, 925, 153
Bianchetti, A., Rodighiero, G., Donevski, D., et al. 2025, arXiv:2507.16917
Blánquez-Sesé, D., Gómez-Guijarro, C., Magdis, G. E., et al. 2023, A&A, 674, A166
Bolatto, A. D., Wolfire, M., & Leroy, A. K. 2013, ARA&A, 51, 207
Boquien, M., Burgarella, D., Roehlly, Y., et al. 2019, A&A, 622, A103
Bradley, L., Sipőcz, B., Robitaille, T., et al. 2024, astropy/photutils: v2.0.2, Zenodo, doi:10.5281/zenodo.13989456
Bruzual, G., & Charlot, S. 2003, MNRAS, 344, 1000
Chabrier, G. 2003, PASP, 115, 763
Charlot, S., & Fall, S. M. 2000, ApJ, 539, 718
Ciesla, L., Buat, V., Boquien, M., et al. 2021, A&A, 653, A6
Cochrane, R. K., Hayward, C. C., & Anglés-Alcázar, D. 2022, ApJL, 939, L27
Damjanov, I., Zahid, H. J., Geller, M. J., Fabricant, D. G., & Hwang, H. S. 2018, ApJS, 234, 21
Davé, R., Anglés-Alcázar, D., Narayanan, D., et al. 2019, MNRAS, 486, 2827
De Vis, P., Jones, A., Viaene, S., et al. 2019, A&A, 623, A5
Donevski, D., Damjanov, I., Nanni, A., et al. 2023, A&A, 678, A35
Donevski, D., Lapi, A., Małek, K., et al. 2020, A&A, 644, A144
Draine, B. T., & Li, A. 2007, ApJ, 657, 810
Dunne, L., Gomez, H. L., da Cunha, E., et al. 2011, MNRAS, 417, 1510
Dunne, L., Maddox, S. J., Papadopoulos, P. P., Ivison, R. J., & Gomez, H. L. 2022, MNRAS, 517, 962
Ellison, S., Huang, Q., Yang, D., et al. 2025, OJAp, 8, 87
French, K. D., Yang, Y., Zabludoff, A. I., & Tremonti, C. A. 2018, ApJ, 862, 2
Gobat, R., Daddi, E., Magdis, G., et al. 2018, NatAs, 2, 239
Gobat, R., D'Eugenio, C., Liu, D., et al. 2022, A&A, 668, L4
Guo, H., Jones, M. G., Wang, J., & Lin, L. 2021, ApJ, 918, 53
Hayashi, M., Tadaki, K.-i., Kodama, T., et al. 2018, ApJ, 856, 118
Hirashita, H., & Nozawa, T. 2017, P&SS, 149, 45
Lee, M. M., Steidel, C. C., Brammer, G., et al. 2024, MNRAS, 527, 9529
Leśniewska, A., Michałowski, M. J., Gall, C., et al. 2023, ApJ, 953, 27
Li, Z., French, K. D., Zabludoff, A. I., & Ho, L. C. 2019, ApJ, 879, 131
Li, Z., Li, Z., Smith, M. W. L., et al. 2020, MNRAS, 492, 195
Lisiecki, K., Donevski, D., Man, A. W. S., et al. 2025, arXiv:2509.10117
Lorenzon, G., Donevski, D., Lisiecki, K., et al. 2025, A&A, 693, A118
Magdis, G. E., Daddi, E., Béthermin, M., et al. 2012, ApJ, 760, 6
Magdis, G. E., Gobat, R., Valentino, F., et al. 2021, A&A, 647, A33
Man, A. W. S., Greve, T. R., Toft, S., et al. 2016, ApJ, 820, 11
McMullin, J. P., Waters, B., Schiebel, D., Young, W., & Golap, K. 2007, ASPC, 376, 127
Michałowski, M. J., Gall, C., Hjorth, J., et al. 2024, ApJ, 964, 129
Morishita, T., Abdurro'uf, Hirashita, H., et al. 2022, ApJ, 938, 144
Nanni, A., Romano, M., Donevski, D., et al. 2025, ApJL, 988, L5
Narayanan, D., Krumholz, M. R., Ostriker, E. C., & Hernquist, L. 2012, MNRAS, 421, 3127
Park, M., Belli, S., Conroy, C., et al. 2023, ApJ, 953, 119
Pistis, F., Pollo, A., Figueira, M., et al. 2024, A&A, 683, A203
Planck Collaboration, Aghanim, N., Akrami, Y., et al. 2020, A&A, 641, A6
Popping, G., Shivaei, I., Sanders, R. L., et al. 2023, A&A, 670, A138
Rodríguez Montero, F., Davé, R., Wild, V., Anglés-Alcázar, D., & Narayanan, D. 2019, MNRAS, 490, 2139
Schreiber, C., Labbé, I., Glazebrook, K., et al. 2018, A&A, 611, A22
Schreiber, C., Pannella, M., Elbaz, D., et al. 2015, A&A, 575, A74
Scoville, N., Sheth, K., Aussel, H., et al. 2016, ApJ, 820, 83
Setton, D. J., Khullar, G., Miller, T. B., et al. 2024, ApJ, 974, 145
Shirley, R., Roehlly, Y., Hurley, P. D., et al. 2019, MNRAS, 490, 634
Shuntov, M., Akins, H. B., Paquereau, L., et al. 2025, arXiv:2506.03243
Siegel, J. C., Setton, D. J., Greene, J. E., et al. 2025, ApJ, 985, 125
Smercina, A., Smith, J.-D. T., French, K. D., et al. 2022, ApJ, 929, 154
Solomon, P. M., & Vanden Bout, P. A. 2005, ARA&A, 43, 677
Speagle, J. S., Steinhardt, C. L., Capak, P. L., & Silverman, J. D. 2014, ApJS, 214, 15
Spilker, J., Bezanson, R., Barišić, I., et al. 2018, ApJ, 860, 103
Spilker, J. S., Whitaker, K. E., Narayanan, D., et al. 2025, ApJL, 993, L40
Stevenson, S. D., Carnall, A. C., Leung, H.-H., et al. 2025, MNRAS,
Suess, K. A., Beverage, A. G., Kriek, M., et al. 2025, arXiv:2506.14361
Suess, K. A., Bezanson, R., Spilker, J. S., et al. 2017, ApJL, 846, L14
Suzuki, T. L., Glazebrook, K., Schreiber, C., et al. 2022, ApJ, 936, 61
Tacconi, L. J., Genzel, R., Saintonge, A., et al. 2018, ApJ, 853, 179
Umehata, H., Kubo, M., & Nakanishi, K. 2025, ApJL, 985, L8
Weibel, A., de Graaff, A., Setton, D. J., et al. 2025, ApJ, 983, 11
Whitaker, K. E., Narayanan, D., Williams, C. C., et al. 2021a, ApJL, 922, L30
Whitaker, K. E., Williams, C. C., Mowla, L., et al. 2021b, Natur, 597, 485
Williams, C. C., Spilker, J. S., Whitaker, K. E., et al. 2021, ApJ, 908, 54
Woodrum, C., Williams, C. C., Rieke, M., et al. 2022, ApJ, 940, 39
Wu, P.-F., Bezanson, R., D'Eugenio, F., et al. 2023, ApJ, 955, 75
Young, L. M., Bureau, M., Davis, T. A., et al. 2011, MNRAS, 414, 940
Zanella, A., Valentino, F., Gallazzi, A., et al. 2023, MNRAS, 524, 923
Zheng, Y., Dave, R., Wild, V., & Montero, F. R. 2022, MNRAS, 513, 27